Chemical Engineering Science 227 (2020) 115927

Contents lists available at ScienceDirect

Chemical Engineering Science

journal homepage: www.elsevier.com/locate/ces

Chain length matters: Structural transition and capacitance of room temperature ionic liquids in nanoporous electrodes

Jie Yang [a], Cheng Lian [a,b,*], Honglai Liu [a]

[a] State Key Laboratory of Chemical Engineering, Frontiers Science Center for Materiobiology and Dynamic Chemistry, Shanghai Engineering Research Center of Hierarchical Nanomaterials, and School of Chemistry and Molecular Engineering, East China University of Science and Technology, Shanghai 200237, China
[b] Institute for Theoretical Physics, Center for Extreme Matter and Emergent Phenomena, Utrecht University, Princetonplein 5, 3584 CC Utrecht, the Netherlands

HIGHLIGHTS

- The interfacial structure changes from monolayer to bilayer with increasing chain length.
- Additional chains can significantly enhance the capacitance in nearly neutral pores.
- Additional chains can dampen the capacitance under negative and positive electrical potential.
- The understanding of the self-assembly of cations in nanoporous electrodes.

GRAPHICAL ABSTRACT

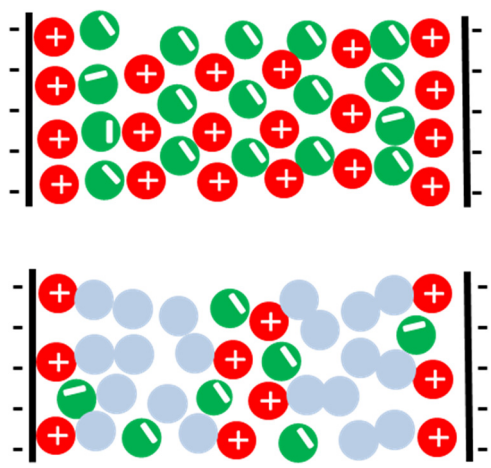

ARTICLE INFO

Article history:
Received 9 April 2020
Received in revised form 17 June 2020
Accepted 19 June 2020
Available online 24 June 2020

Keywords:
Room-temperature ionic liquids
Interfacial structure
Capacitive performance
Chain length effect

ABSTRACT

Room-temperature ionic liquids (RTILs) have shown great potential in promoting the widespread application of energy storage devices. The relationship between the electrical double layer (EDL) structure and capacitive performance of different RTILs is vital to the rational design of novel RTIL electrolytes. Herein, we have investigated the microscopic structures of three types of RTILs containing cations with varying tail lengths in nanopores, their charging behaviors, and their EDL capacitances using classical density functional theory (CDFT). The results show that the interfacial structure changes from a monolayer to a bilayer as the neutral chain length of the cations increases, which is in agreement with previous experimental results (Smith et al., 2013). Moreover, the RTILs containing cations with longer chains can significantly enhance the capacitance in nearly neutral pores, while they dampen capacitance under negative electrical potential and show little disadvantage when positive potential is applied.

1. Introduction

Supercapacitors, also known as electric double-layer capacitors (EDLCs), store electrical energy through the physisorption of ions on the surfaces of porous electrodes (Adusei et al.,

* Corresponding author.
E-mail address: liancheng@ecust.edu.cn (C. Lian).

https://doi.org/10.1016/j.ces.2020.115927
0009-2509/

2020; Zhong et al., 2015; Jiang and Wu, 2013; Shao et al., 2015; Fedorov and Kornyshev, 2014; Frackowiak et al., 2013). Unlike an electric double layer (EDL) formed near a planar metallic electrode, supercapacitors typically utilize porous electrodes with a broad range of morphologies and pore-size distributions (Burt et al., 2014; Frackowiak et al., 2013; Simon and Gogotsi, 2013; Simon and Gogotsi, 2008; Dou et al., 2017; Lian et al., 2020), which can significantly influence the ion distribution near the surface of the solid electrode. Many investigations have demonstrated the effects of pore size on the structure of the EDL, the capacitance, and ion transport both experimentally and theoretically (Jiang and Wu, 2013; Feng et al., 2009; Largeot et al., 2008). For instance, EDLC capacitance shows an anomalous increase when the pore size is in the range of the dimensionality of the ionic species, suggesting that electrodes with subnanometer pores are a better choice than those with larger pores (Chmiola et al., 2006).

Similar studies have been done for the selection of electrolytes, where room-temperature ionic liquids (RTILs) have demonstrated superior performance compared with traditional electrolytes (aqueous/organic). Previous studies showed that RTILs provide wide electrochemical windows, exhibit excellent thermal stability and are nonvolatile (Seddon, 1997). Inspired by this, a variety of RTILs have been used in EDL capacitors with porous carbon electrodes (Largeot et al., 2008). Comprehensive understanding of ion distributions near the solid electrode surface for different RTILs and how transitions in the interfacial structural influence the charging behavior are beneficial for supercapacitor performance. In recent years, a resurgence in the viability of ionic liquids has been seen due to continuing efforts in characterizing a wide plethora of the available ionic liquids. However, much of this characterization has focused on the ionic liquids themselves rather than their properties near the solid electrode/electrolyte interface (Valderrama and Rojas, 2009).

Herein, we have investigated the interfacial structural transitions and charge behavior of RTILs containing different imidazolium cations with varying tail lengths based on classical density functional theory (CDFT). Increasing numbers of studies have suggested that CDFT is able to describe the thermodynamic properties of electrified solid/ionic liquid interfaces (Forsman et al., 2011; Szparaga et al., 2012; Shrivastav et al., 2018; Liu et al., 2018), which allows proper understanding of how the tail length influences the interfacial structure and capacitance for both positive and negative electrode potentials while avoiding any issues caused by asymmetry in sphere sizes (Lian et al., 2018). A previous study by Gallegos et al. (2019) showed the different influences of the side alkyl chains of imidazolium cations on the electric double layer (EDL) capacitance of planar electrodes and microporous electrodes. To evaluate the influence the neutral alkyl chains of the cations have on the interfacial structure and capacitance of porous EDLCs, without changing their overall physicochemical properties, we considered three cations which all share the same cation head but have varying neutral alkyl segment length. Specifically, these three ILs contain a tetrafluoroborate anion and either 1-methyl-3-ethylimidazolium (EMIM), 1-methyl-3-buytlimidazolium (BMIM), or 1-methyl-3-hexylimidazolium (HMIM) cations, respectively.

This paper is structured as follows. First, a description of the coarse-grained model for RTILs containing cations with varying tail lengths and porous electrodes and a brief introduction to the CDFT method used in this work are given. Next, we discuss the effects of neutral chain length on the EDL structure and capacitive performance. Finally, we summarize the main results and implications for possible future studies.

2. Model and methods

2.1. Molecular model

Fig. 1 shows the coarse-grained schematic for the RTIL model. Similar to previous studies (Jiang et al., 2011; Wu et al., 2011), the ions were modeled as identical sized hard spheres with each cation having a neutral segment attached to the cation of varying lengths (n = 0, 1, and 2) to represent EMIM, BMIM, and HMIM, respectively. This model is capable of accounting for not only electrostatic correlations and ionic excluded volume effects but also for the structure transitions that are important for EDL capacitive performance. Parameters such as monomer size and approximate charge were selected based on 1-ethyl-3-methylimidazolium bis-(trifluoromethanesulfonyl)imide (EMI-TFSI), a RTIL commonly used in electrochemical devices. Specifically, each hard sphere diameter for the cations was fixed at $\sigma_+ = 0.5$ nm, and the diameter of the anion ($TFSI^-$) was also fixed at 0.5 nm. The temperature was set to 298 K.

A nanoporous electrode was represented by the slit model. The nonelectrical component of the interaction between the electrode and the sphere particle, i, is modeled as a hard-wall potential $V_i(z)$.

$$V_i(z) = \begin{cases} \infty, & z < \frac{\sigma_i}{2} \text{ or } z > H - \frac{\sigma_i}{2} \\ 0, & \text{otherwise} \end{cases} \tag{1}$$

where H is the surface-to-surface separation (or the pore width), and z is the perpendicular distance from the surface, and σ_i is the diameter of the sphere particle i.

2.2. Classical density functional theory

The details of the CDFT calculations can be found in previous publications (Kumaravadivel and Evans, 1975; van Roij et al., 1999; Wu, 2006). It is assumed that the density profiles only vary in the z direction, i.e., the direction perpendicular to the surface of the nanopore electrode. At a given temperature T and a bulk ionic species density, CDFT can predict the one-dimensional density profiles of cations (M) and anions (a) across a slit pore by minimizing the grand potential

$$\begin{aligned} \beta\Omega[\rho_M(\mathbf{R}), \{\rho_a(\mathbf{r})\}] = \beta F[\rho_M(\mathbf{R}), \{\rho_a(\mathbf{r})\}] \\ + \int [\beta\Psi_M(\mathbf{R}) - \beta\mu_M]\rho_M(\mathbf{R})d\mathbf{R} + \sum_a \\ \times \int [\beta\Psi_a(\mathbf{r}) - \beta\mu_a]\rho_a(\mathbf{r})d\mathbf{r} \end{aligned} \tag{2}$$

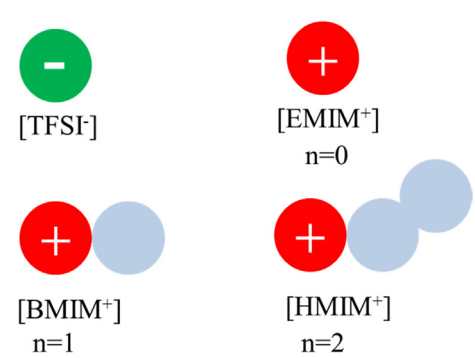

Fig. 1. Schematic for the RTILs considered in this work. Ions are assumed to be charged hard spheres with neutral segments of varying length attached to the cations to represent EMIM (n = 0), BMIM (n = 1), and HMIM (n = 2), respectively.

where $\beta^{-1} = k_B T$, $R \equiv (\boldsymbol{r}_1, \boldsymbol{r}_2, \cdots \boldsymbol{r}_m)$ represents the coordinates specifying the positions of m hard spheres of each cation, μ_a and μ_M are the chemical potentials of the anions and cations, respectively. $\Psi_a(\boldsymbol{r})$ stands for the external potential for the anions, $\Psi_m(\boldsymbol{R})$ summarizes the external potential for the cations, which is expressed as $\Psi_M(\boldsymbol{R}) = \sum_{i=1}^{m} \varphi_i(\boldsymbol{r}_i)$, and F denotes the total intrinsic Helmholtz energy. The intrinsic Helmholtz energy F consists of an ideal-gas contribution and an excess contribution from the intermolecular interactions F^{ex}

$$\beta F = \int [ln\rho_M(\mathbf{R}) - 1]\rho_M(\mathbf{R})d\mathbf{R} + \beta \int V_b(\mathbf{R})\rho_M(\mathbf{R})d\mathbf{R} + \sum_a \int [ln\rho_a(\mathbf{r}) - 1]\rho_a(\mathbf{r})d\mathbf{r} + \beta F^{ex} \tag{3}$$

where V_b represents the bonding potential of the cations.

Minimizing the grand potential Ω with the decomposition of the ideal part and the nonideal part of Helmholtz free energy as shown in Eq. (2), we obtain a set of Euler-Lagrange equations for a segmental density distribution of polymers and monomers,

$$\rho_M(\boldsymbol{R}) = \exp\left[\beta\mu_M - \beta V_b(\boldsymbol{R}) - \beta\Psi_M(\boldsymbol{R}) - \frac{\delta\beta F^{ex}}{\delta\rho_M(\boldsymbol{R})}\right] \tag{4}$$

$$\rho_a(\boldsymbol{r}) = \exp\left[\beta\mu_a - \beta\Psi_a(\boldsymbol{r}) - \frac{\delta\beta F^{ex}}{\delta\rho_a(\boldsymbol{r})}\right] \tag{5}$$

The total number densities of the positive and neutral segments of the cations can be obtained from

$$\rho_m(\boldsymbol{r}_m) = \int d\boldsymbol{R}\delta(\boldsymbol{r} - \boldsymbol{r}_m)\rho_M(\boldsymbol{R}) \tag{6}$$

where the positive segments account for $1/m$.

2.3. Excess free energy functional

The excess Helmholtz free energy F^{ex} can be decomposed into several contributions due to different molecular interactions and correlations. For the system considered here,

$$F^{ex} = F^{ex}_{hs} + F^{ex}_{ch} + F^{ex}_{C} + F^{ex}_{el} + F^{ex}_{att} \tag{7}$$

where F^{ex}_{hs},F^{ex}_{ch},F^{ex}_{C},F^{ex}_{el} and F^{ex}_{att} represent the excess Helmholtz free energy ascribed to hard sphere repulsion, chain connectivity, direct Coulombic energy, electrostatic correlations and long-range attractions, respectively. The excess chemical potential is expressed as the functional derivative of the excess Helmholtz free energy with respect to the density profile,

$$\mu^{ex}(\boldsymbol{r}) = \frac{\delta F^{ex}}{\delta\rho(\boldsymbol{r})} = \mu^{ex}_{hs}(\boldsymbol{r}) + \mu^{ex}_{ch}(\boldsymbol{r}) + \mu^{ex}_{C}(\boldsymbol{r}) + \mu^{ex}_{el}(\boldsymbol{r}) + \mu^{ex}_{att}(\boldsymbol{r}) \tag{8}$$

where $\mu^{ex}_{hs}(\boldsymbol{r})$, $\mu^{ex}_{ch}(\boldsymbol{r})$, $\mu^{ex}_{C}(\boldsymbol{r})$, $\mu^{ex}_{el}(\boldsymbol{r})$, and $\mu^{ex}_{att}(\boldsymbol{r})$ are the excess chemical potential due to corresponding excess Helmholtz free energies.

2.3.1. Hard-core repulsion by fundamental measure theory

For a mixture of hard spheres, the hard sphere potential between two spherical particles is given by

$$\beta u(\mathbf{r}_i, \mathbf{r}_j) = \begin{cases} 0, & |\mathbf{r}_i - \mathbf{r}_j| \geqslant \frac{1}{2}(\sigma_i + \sigma_j) \\ \infty, & |\mathbf{r}_i - \mathbf{r}_j| < \frac{1}{2}(\sigma_i + \sigma_j) \end{cases} \tag{9}$$

where $\boldsymbol{r}_i$ and $\boldsymbol{r}_j$ represent the spatial positions of particle i and j, respectively, and σ_i and σ_j are the corresponding diameters.

In the fundamental measure theory (FMT) proposed by Rosenfeld (Rosenfeld, 1989), the excess free energy is expressed as

$$\beta F^{ex}_{hs} = \int d\boldsymbol{r}\Phi(\{n_\alpha(\boldsymbol{r})\}) \tag{10}$$

where $\Phi(\{n_\alpha(\boldsymbol{r})\})$ is the reduced excess free energy density which is represented by

$$\Phi(\{n_\alpha(\boldsymbol{r})\}) = -n_0 \ln(1 - n_3) + \frac{n_1 n_2 - \boldsymbol{n}_{V1} \cdot \boldsymbol{n}_{V2}}{1 - n_3} + \frac{n_2^3/3 - n_2 \boldsymbol{n}_{V2} \cdot \boldsymbol{n}_{V2}}{8\pi(1 - n_3)^2} \tag{11}$$

in the original FMT, and

$$\Phi(\{n_\alpha(\boldsymbol{r})\}) = -n_0 \ln(1 - n_3) + \frac{n_1 n_2 - \boldsymbol{n}_{V1} \cdot \boldsymbol{n}_{V2}}{1 - n_3} + (n_2^3 - 3n_2 \boldsymbol{n}_{V2} \cdot \boldsymbol{n}_{V2}) \frac{n_3 + (1 - n_3)^2 \ln(1 - n_3)}{36\pi n_3^2 (1 - n_3)^2} \tag{12}$$

in the modified FMT.

And $n_\alpha(\boldsymbol{r})$ are a set of weighted densities defined as

$$n_\alpha(\boldsymbol{r}) = \sum_i n_{\alpha,i}(\boldsymbol{r}) = \sum_i \int d\boldsymbol{r}' \rho_i(\boldsymbol{r}')\omega_i^\alpha |\boldsymbol{r} - \boldsymbol{r}'| \tag{13}$$

with $\alpha = 0, 1, 2, 3, V1, V2$, and the summation is over all species in the system. In addition, $\omega_i^{(\alpha)}$ represents six weighted functions given by (Yu and Wu, 2002a), which are independent of the density profiles but directly related to the geometry of the spherical particle.

In the silt pore geometry, $\rho(\boldsymbol{r})$ is homogeneous in the plane parallel to the confining surface and then $\rho(\boldsymbol{r}) = \rho(z)$, with z being the component of $\mathbf{r}$ in the z-direction, therefore, the weighted densities are given by

$$\begin{aligned} n_2(z) &= \int d\boldsymbol{r}' \rho(\boldsymbol{r}')\omega^{(2)}(|\boldsymbol{r} - \boldsymbol{r}'|) \\ &= \int_{-\infty}^{\infty} dx' \int_{-\infty}^{\infty} dy' \int_{-\infty}^{\infty} dz' \rho(z')\delta\left(\tfrac{\sigma}{2} - \sqrt{(x - x')^2 + (y - y')^2 + (z - z')^2}\right) \\ &= \pi \int_{-\infty}^{\infty} dz' \rho(z') \int_0^{\infty} dt \delta\left(\tfrac{\sigma}{2} - \sqrt{t + (z - z')^2}\right) \\ &= \pi \int_{-\infty}^{\infty} dz' \rho(z') \int_{-\infty}^{\sigma/2 - |z - z'|} ds(\sigma - 2s)\delta(s) \\ &= \pi\sigma \int_{-\infty}^{\infty} dz' \rho(z') \int_{-\infty}^{\sigma/2 - |z - z'|} ds\delta(s) \\ &= \pi\sigma \int_{z - \sigma/2}^{z + \sigma/2} dz' \rho(z') \end{aligned} \tag{14}$$

Similar to the calculation for $n_2(z)$, the one-dimensional weighted densities for $\alpha = 0, 1, 3, V1, V2$ and the excess free energy due to hard sphere repulsion can be obtained subsequently.

2.3.2. Van de Waals attraction by square well interaction

The Van der Waals attraction between spherical particles is described by a Square-Well (SW) potential $u^{att(r)}_{i,j} = -\varepsilon_{i,j}$ for $r < \lambda_{i,j}$ (Jin et al., 2011). Here, the attractive energy, or the attraction well depth, is set as $\varepsilon_{i,j} = 1k_BT$, and the attractive range $\lambda_{i,j}$ is set as 2σ.

The excess free energy function due to the van der Waals attraction is approximated by the mean-field approximation,

$$\beta F^{ex}_{att} = \frac{1}{2} \sum_i \sum_j \int d\mathbf{r} d\mathbf{r}' u^{att}_{i,j}(|\mathbf{r} - \mathbf{r}'|)\rho_i(\mathbf{r})\rho_j(\mathbf{r}') \tag{15}$$

and then the excess chemical potential due to the attractive force is

$$\beta\mu^{ex}_{i,att}(\mathbf{r}) = \frac{\delta\beta F^{ex}_{att}}{\delta\rho_i(\mathbf{r})} = \sum_j \int d\mathbf{r}' u^{att}_{i,j}(|\mathbf{r} - \mathbf{r}'|)\rho_j(\mathbf{r}') \tag{16}$$

For the silt pore case, we have

$$\begin{aligned}\beta\mu^{ex}_{i,att}(z) &= \sum_j \int d\mathbf{r}' u^{att}_{i,j}(|\mathbf{r}-\mathbf{r}'|)\rho_j(\mathbf{r}') \\ &= \sum_j \int dx' \int dy' \int dz' u^{att}_{i,j}(|z'|)\rho_j(z-z') \\ &= \pi \sum_j \int dz' \rho_j(z-z') \int_0^\infty dt u^{att}_{i,j}(s)(\sqrt{z'^2+t}) \\ &= 2\pi \sum_j \int dz' \rho_j(z-z') \int_{z'}^\infty s u^{att}_{i,j}(s) ds \\ &= -2\pi \sum_j \int_{-\lambda_{i,j}}^{\lambda_{i,j}} dz' \varepsilon_{i,j} \rho_j(z-z')(\lambda^2_{i,j} - z'^2)\end{aligned} \tag{17}$$

2.3.3. Direct electrostatic potential – Coulombic interactions

The excess free energy due to the direct electrostatic potential of the system is expressed as

$$\beta F^{ex}_C = \frac{l_B}{2} \sum_{i,j} d\mathbf{r} d\mathbf{r}' \frac{Z_i Z_j \rho_i(\mathbf{r}) \rho_j(\mathbf{r}')}{|\mathbf{r}-\mathbf{r}'|} \tag{18}$$

where $l_B = \beta e^2/(\varepsilon_r \varepsilon_0)$ is the Bjerrum length, ε_0 is the permittivity of free space, Z_i and Z_j are the valence of the ionic species i and j, respectively. Throughout this work, both the anions and cations are assumed to be monovalent (−1 and +1). Anytime that ionic species are explicitly considered in this work, a residual dielectric constant ($\varepsilon_r = 2$) was adopted to account for the effective electronic polarizability of ILs in the silt pore, which is in agreement with previous studies on ILs and their experimental results (Fedorov and Kornyshev, 2008a; Izgorodina et al., 2009; Kondrat and Kornyshev, 2011; Fedorov and Kornyshev, 2014; Kondrat and Kornyshev, 2016).

It has been hypothesized that the polarizability effect and the image charge effect are relatively unimportant for the formation of electrolyte-electrode interface structures since the residual dielectric constant for a typical ionic liquids is similar to the dielectric constant of carbon electrodes (Kondrat and Kornyshev, 2011; Kondrat et al., 2011; Wang, 2016). Specifically, the effect of a sharp dielectric discontinuity occurring between the surface and the ionic liquid can be quantified by the image factor $\Delta_s = (\varepsilon_s - \varepsilon_r)/(\varepsilon_s - \varepsilon_r)$ where ε_s and ε_r are the surface and liquid dielectric permittivity, respectively. Due to the similarity of the dielectric constants of the carbon electrode and the ionic liquid, the factor evaluating the polarizability or electronic screening effect is close to zero.

To avoid numerical problems, the electrostatic potential of the system satisfies the Poisson equation

$$\nabla^2 \psi(\mathbf{r}) = -\frac{4\pi e}{\varepsilon} \sum_i \rho_c(\mathbf{r}) \tag{19}$$

with the charge being $\rho_c(\mathbf{r}) = \sum Z_i \rho_i(\mathbf{r})$ and appropriate boundary conditions. We can further obtain the summation of the direct Coulombic interactions and the external field (charge surface) as

$$\beta(F^{ex}_C + \Psi_{ext}) = \int d\mathbf{r} \sum_i e Z_i \rho_i(\mathbf{r}) \psi(\mathbf{r}) \tag{20}$$

with the corresponding excess chemical potential as

$$\beta\mu^{ex}_{i,C}(\mathbf{r}) = e Z_i \psi(\mathbf{r}) \tag{21}$$

For a silt pore geometry, where the density profiles are homogeneous in both the x- and y-directions, we have

$$\frac{d^2\psi(z)}{dz^2} = -\frac{4\pi e}{\varepsilon} \rho_c(z) \tag{22}$$

i.e.,

$$\begin{aligned}&\frac{d\psi(z)}{dz} - \frac{d\psi(z)}{dz}\Big|_{H/2} = -\frac{4\pi e}{\varepsilon} \int_{H/2}^z dz_2 \rho_c(z_2) \\ &\Rightarrow \frac{d\psi(z)}{dz} = \frac{d\psi(z)}{dz}\Big|_{H/2} - \frac{4\pi e}{\varepsilon} \int_{H/2}^z dz_2 \rho_c(z_2) \\ &\Rightarrow \psi(z) - \psi_{H/2} = (z - H/2)A_{H/2} - \frac{4\pi e}{\varepsilon} \int_{H/2}^z dz_1 \int_{H/2}^{z1} dz_2 \rho_c(z_2) \\ &\Rightarrow \psi(z) = \psi_{H/2} + (z - H/2)A_{H/2} + \frac{4\pi e}{\varepsilon} \int_z^{H/2} dz'(z-z')\rho_c(z')\end{aligned} \tag{23}$$

where $A_{H/2} \equiv d\psi(z)/dz|_{H/2}, \psi_{H/2} \equiv \psi(z = H/2)$. When $z = 0$, we have

$$\psi_0 \equiv \psi(z=0) = \psi_{H/2} - HA_{H/2} - \frac{4\pi e}{\varepsilon} \int_0^{H/2} dz' z' \rho_c(z') \tag{24}$$

Thus, Eq. (23) can be written as

$$\psi(z) = \psi_0 + zA_{H/2} - \frac{4\pi e}{\varepsilon}[zQ + \int_0^z dz'(z-z')\rho_c(z')] \tag{25}$$

where $Q = -\int_0^{H/2} dz' \rho_c(z')$ is the surface charge density.

For a system confined between two parallel walls, we obtain the boundary conditions $\psi(z = H/2) = \psi_{H/2}$ and $\psi(z = 0) = \psi_0$, therefore

$$A_{H/2} = \frac{1}{H/2}[\psi_R - \psi_0 - \frac{4\pi e}{\varepsilon} \int_0^{H/2} dz' z' \rho_c(z')] \tag{26}$$

and thus,

$$\begin{aligned}\psi(z) = \psi_0 + \frac{z}{H/2}[\psi_{H/2} - \psi_0 + \frac{4\pi e}{\varepsilon} \int_0^{H/2} dz'(H/2 - z')\rho_c(z')] \\ - \frac{4\pi e}{\varepsilon} \int_0^Z dz'(z-z')\rho_c(z')\end{aligned} \tag{27}$$

2.3.4. Electrostatic correlation

Here, the excess Helmholtz free energy due to electrostatic correlation F^{ex}_{el} is approximated by a quadratic functional Taylor expansion with respect to that of a monomeric bulk fluid of density $\{\rho^b_i\}$,

$$\begin{aligned}\beta F^{ex}_{el}[\{\rho_i(\mathbf{r})\}] = \beta F^{ex}_{el}[\{\rho_{i,b}\}] + \sum_i \beta\mu^{ex}_{el,i} \int d\mathbf{r}[\rho_i(\mathbf{r}) - \rho_{i,b}] \\ -\frac{1}{2}\sum_i \sum_j \int d\mathbf{r}_1 d\mathbf{r}_2 [\rho_i(\mathbf{r}_1) - \rho_{i,b}] C^{el}_{i,j}(|\mathbf{r}_1 - \mathbf{r}_2|)[\rho_j(\mathbf{r}_2) - \rho_{j,b}]\end{aligned} \tag{28}$$

where $\beta\mu^{ex}_{el,i} \equiv \delta F^{ex}_{el}[\{\rho_i(\mathbf{r})\}]/\delta\rho_i(\mathbf{r})|_{\rho_i(\mathbf{r})=\rho_{i,b}}$ represents the bulk excess chemical potential of species i due to the electrostatic correlation, and $C^{el}_{i,j}(|\mathbf{r}_1 - \mathbf{r}_2|)$ is the DCF of the electrostatic correlation and approximated by Yu et al. (2004).

For the silt pore case, $\beta\mu^{ex}_{el,i}(\mathbf{r})$ is only dependent on the z-direction, and therefore

$$\begin{aligned}\beta\mu^{ex}_{el,i}(\mathbf{r}) &= -\sum_j \int d\mathbf{r}' \rho_j(\mathbf{r}-\mathbf{r}') C^{el}_{i,j}|\mathbf{r}'|] \\ &= -\pi \sum_j \int_{-\infty}^{\infty} dz' \rho_j(z-z') \int_0^\infty dt C^{el}_{i,j}(\sqrt{z'^2+t}) \\ &= -2\pi \sum_j \int_{-\infty}^{\infty} dz' \rho_j(z-z') \int_{z'}^\infty ds C^{el}_{i,j}(s) \\ &= -2\pi \sum_j \int_{-(\sigma_i+\sigma_j)/2}^{(\sigma_i+\sigma_j)/2} dz' \rho_j(z-z') \int_{z'}^{(\sigma_i+\sigma_j)/2} ds C^{el}_{i,j}(s)\end{aligned} \tag{29}$$

2.3.5. Chain connectivity by first-order perturbation theory

The excess Helmholtz free energy due to chain connectivity for polymeric fluids can be described by perturbation theory using the corresponding monomeric system as a reference. For uniform systems, the thermodynamic perturbation theory (TPT) was first pro-

posed by Wertheim (Wertheim, 1984) using monomeric hard-sphere fluids as reference to study the associating hard-sphere molecules. Although there are many different versions of TPT, we have a brief derivation of the extension of the first-order thermodynamic perturbation theory (TPT1) for inhomogeneous systems.

$$\beta\mu^{ex}_{ch,t}(\mathbf{r}) = \frac{\delta\beta F^{ex}_{ch}}{\delta\rho_t(\mathbf{r})} = \sum_{\alpha}\int d\mathbf{r}' \frac{\partial\Phi^{ex}_{ch}}{\partial n_{\alpha,t}(\mathbf{r}')}\omega^{(\alpha)}_t(\mathbf{r}'-\mathbf{r}) \tag{30}$$

where Φ^{ex}_{ch} is the free energy density due to the chain connectivity. Unlike in Section 2.3.1, $n_{\alpha,t}(\mathbf{r})$ in Eq. (30) is not the total weighted density but the weighted density of t-th specie. The detailed equations for our system can be found in the literature (Li and Wu, 2006a; Li and Wu, 2006b)

2.4. Numerical methods

For a silt pore system, where the density profile is only z dependent, the density distributions of the anions and segments of the cations are given by

$$\rho_a(z) = \exp\left[\beta\mu_a - \beta\Psi_a(z) - \frac{\partial\beta F^{ex}}{\partial\rho_a(z)}\right] \tag{31}$$

$$\rho_m(z) = \exp(\beta\mu_M)\sum_{j=1}^{M}\exp[-\beta\lambda_m(z)]G^i(z)G^{M+1-i}(z) \tag{32}$$

where the propagator function $G^i(z)$ is determined from the recurrence relation

$$G^i(z) = \int dz\prime \exp[-\beta\lambda_m(z\prime)]\frac{\theta(\sigma_p - |z - z\prime|)}{2\sigma_p}G^{i-1}(z') \tag{33}$$

for $i = 2, ..., M$ with $G^1(z) = 1$, and $\lambda_m(z)$ representing an effective one-body potential.

In this work, the density profiles of the polymer segments and the monomers were solved by the conventional Picard iteration method (Yu and Wu, 2002b). We assigned the bulk concentration as an initial guess for the density profiles of the polymers and monomers. Subsequently, the excess Helmholtz free energy $F^{ex}_i(z)$ and the local electrical potential $\Psi_i(z)$ for each ionic species and the function $G^i(z)$ can be calculated from the initial guess and the boundary conditions. Then, we replaced the values in Eqs. (31) and (32) to acquire a new set of ionic profiles for the next iteration, which stopped when the procedure resulted in unit convergence ($\left|\frac{\Delta\rho_i}{\rho^i_o}\right| < 10^{-4}$ at all positions).

2.5. Amount of excess adsorption and capacitance

From the ion distributions and the electrical potential profiles, we can calculate the excess adsorption number of different ions inside pores by

$$\Gamma^{ex}_i = \int_0^H (\rho_i(z) - \rho_{i,b})dz \tag{34}$$

We can also obtain the surface charge density (Q) according to the overall charge neutrality condition,

$$Q = -\sum_i Z_i e\int_0^{H/2} dz\rho_i(z) \tag{35}$$

Subsequently, the capacitance can be expressed as the derivative of the surface charge density with respect to the electrode potential (Lian et al., 2016b)

$$C_d = \frac{\partial Q}{\partial\psi} \tag{36}$$

3. Results and discussion

We investigated both the interfacial EDL structures, the charging mechanism, and the EDL capacitances of RTILs with different cation chain lengths in a 4.00 nm nanoscale pore for varying surface electrical potentials.

3.1. RTILs in neutral pores

We first consider the effect of chain length on the EDL structures in a neutral pore with surface potential $\psi = 0$. Similar to the previous theoretical (Wu et al., 2011; Lian et al., 2016b) and experimental results (Mezger et al., 2008), the density profiles of the cations and anions in the symmetric RTILs containing EMIM are identical, as shown in Fig. 2a, where a homogeneous mean potential profile is observed throughout the pore (the blue line in Fig. 3). For cations with a neutral side chain, the symmetry between the ions is broken which leads to different density profiles (Lian et al., 2016b; Lian et al., 2017). Though the cation and anion can both occupy the first layer, there is now a hindrance on the cation because of the neutral sphere. This explains why there is a decrease in the presence of the cation near the wall when compared to the presence of the anion (Fig. 2b). The outcome of the electrical potential profiles near the wall are shown by the red and black lines in Fig. 3. Since the first layer has an inhomogeneous potential profile, the second layer compensates for this, and then the next layer compensates, and so forth. This causes an oscillation in electrical potential profile due to imbalances in the charge (that is to say the charge neutrality condition is no longer satisfied) of a neutral pore, which is not seen for the symmetric system. These oscillations are very weak compared to those seen in a charged pore (to be discussed later) and the RTIL within the pore approaches bulk-like behavior after the first few layers from the wall. For HMIM, the chain is sufficiently long and a layer of the neutral segments occurs that was not seen in BMIM due to the Van der Waals forces between the neutral chains during the experiment (Smith et al., 2013; Smith et al., 2014) (Fig. 2c). The neutral segments forming this new layer occupy the space so that the ions move away either side. Since the chain is longer, the electrical potential profile near the wall is amplified due to the increasing hindrance for cations entering the pore, which explains the electrical potential increase that occurs when BMIM was changed to HMIM in Fig. 3. This shows how this layer interrupts the layering of ions, and the positive charge is not fully balanced by the anions.

3.2. RTILs in negative pores

The layer-by-layer structure for RTILs containing EMIM within a negatively charged pore ($-\psi$) can be seen in Fig. 4a, which has been documented previously (Mezger et al., 2008; Fedorov and Kornyshev, 2008b; Bazant et al., 2011). The formation of layers is vital for understanding ionic liquids and their unique properties that are exhibited in the charging mechanism compared with aqueous and organic systems. As shown in Fig. 4, the addition of a chain disrupts the layering of ions that is normally seen for symmetrical ionic liquids. Since the neutral segments need to occupy the space surrounding the cation such that they take the spot where an anion normally would be in if there was no tail by shifting the anions to a new location. When the chain is short, the neutral segment shifts the anions away from the wall. This can be seen in both Fig. 4b and the red line of Fig. 5, by the electrical potential profiles of the first layer being more balanced than the potential profiles of the symmetric system. When the chain is longer, the Van der Waals force discussed previously will dictate the arrangement of ions and the formation of a neutral layer will occur. This is

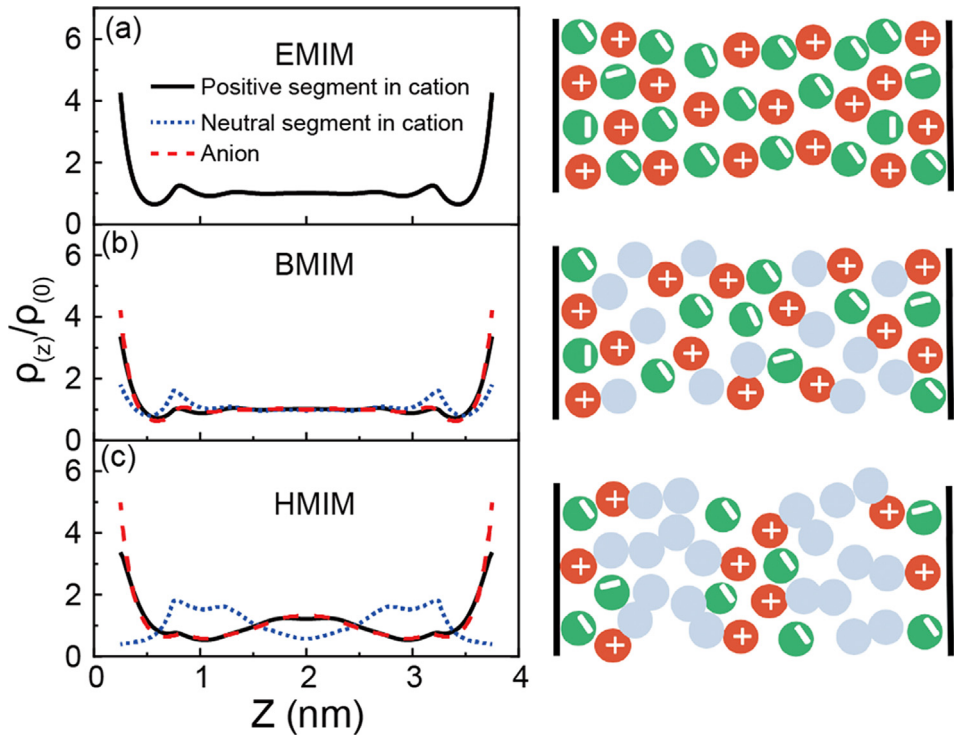

Fig. 2. Density profiles of anions (red dashed line) and the positive (black solid line) and neutral (blue dotted line) segments of cations inside a nanopore at an electrical surface potential of 0 *V* for RTILs containing EMIM (a), BMIM (b), and HMIM (c). (For interpretation of the references to colour in this figure legend, the reader is referred to the web version of this article.)

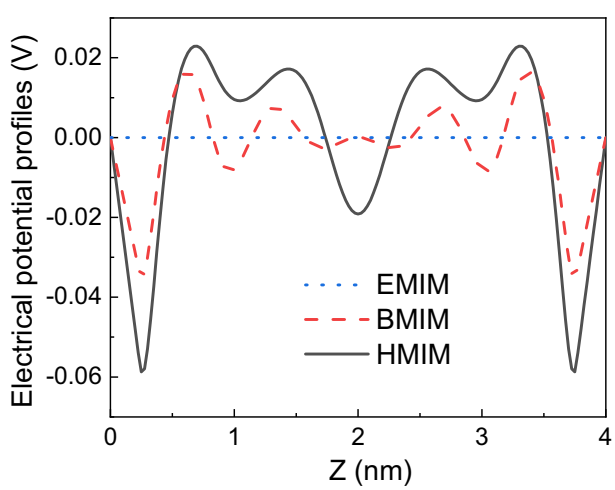

Fig. 3. Electrical potential profiles inside a nanopore at an electrical surface potential of 0 *V* for RTILs containing EMIM (blue dotted line), BMIM (red dashed line), and HMIM (black solid line). (For interpretation of the references to colour in this figure legend, the reader is referred to the web version of this article.)

the case seen in Fig. 4c where the anions are shifted towards the wall instead of away from the wall like for BMIM. As a result, the oscillation of charge smooths as shown by comparison of the curves in Fig. 4 and the pore approaches the bulk condition much faster than the symmetrical system.

3.3. RTILs in positive pores

When the pore is charged positively (ψ) for a symmetric system, the resulting density profile is identical to that of $-\psi$ except the ions are switched (Fig. 6a). However, the structure for cations with chains is significantly different than the structure seen previously for the negatively charged pore (Fig. 4b and c) because the first layer is no longer composed of ions with chains. The orientation of the BMIM/HMIM is most likely to be perpendicular with the cation head being the closest due to the same reason that the layering occurs, which is confirmed in Fig. 6b and c. As mentioned previously, the neutral segment dampens the oscillation of charge (seen in Fig. 7) and allows bulk-like behavior to be approached much sooner than the symmetric system. In addition, similar to Fig. 4c, the neutral segments of the HMIM will form a distinct layer in Fig. 6c due to the attraction between the neutral chains.

3.4. Chain length effects on the charging mechanism

Here, we investigated the charging mechanisms by observing how the excess adsorption of ions inside the nanopore changed with respect to ψ(Fig. 8). To begin, let us first consider the pore with symmetry between the ions (EMIM; Fig. 8a). By observation of the changes in coions and counterions in Fig. 8a, we see that as the pore begins to charge, the counterions increase at the same rate that the coions decrease. This would imply that the ion exchange mechanism is at play which refers to the swapping of counterions with coions. However, once the pore becomes sufficiently charged, ion exchange will be less frequent as the coions are relatively depleted near the wall. This can be seen by the leveling off of the coions in Fig. 8a as the surface becomes highly charged. However, the counterions are continuing to increase in presence in the pore, which implies counterion adsorption is the main charging mechanism.

As shown in Fig. 8b and c, the charging mechanisms for RTILs containing cations with neutral chains of different length are similar to that of EMIM, being dominated by ion exchange at nearly neu-

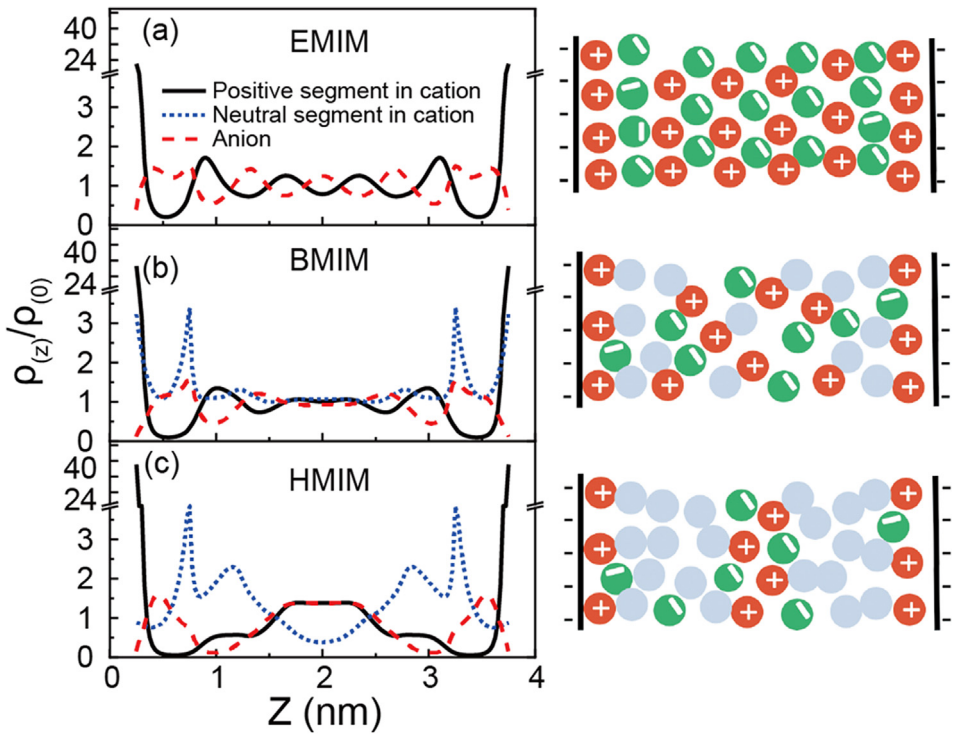

Fig. 4. Density profiles of anions (red dashed line) and the positive (black solid line) and neutral (blue dotted line) segments of cations inside a negatively charged nanopore at the electrical surface potential of $-\psi$ for RTILs containing EMIM (a), BMIM (b), and HMIM (c). (For interpretation of the references to colour in this figure legend, the reader is referred to the web version of this article.)

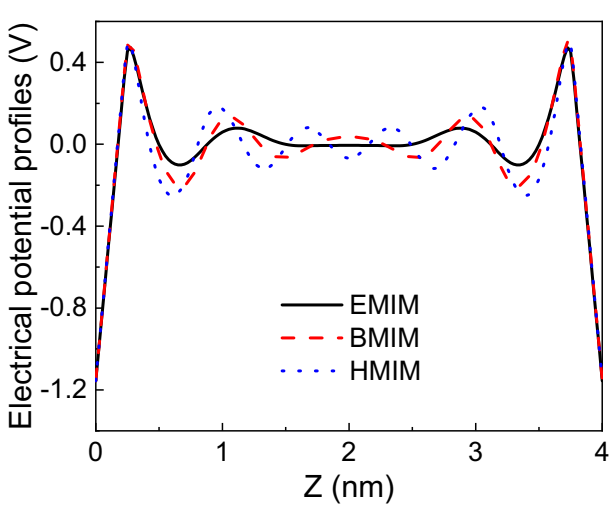

Fig. 5. Electrical potential profiles inside a negative nanopore at the electrical surface potential of $-\psi$ for RTILs containing EMIM (blue dotted line), BMIM (red dashed line), and HMIM (black solid line). (For interpretation of the references to colour in this figure legend, the reader is referred to the web version of this article.)

tral condition and then counterions adsorption at high charged potential. Consistent with previous experimental studies under varying electrical potentials inside nanopores (Chu et al., 2016), the layer thickness increased rapidly with voltage and the "crowding" of ions appeared near the interface. Notably, the variation rate for the anions is nearly two times larger than that for BMIM and three times that for HMIM under small voltage. This is due to the need to replace two anions for BMIM and three for HMIM when the ion exchange does occur.

3.5. Chain length effects on the capacitive performances

Full comprehension of the different mechanisms at varying surface electrical potentials ($-\psi$,0,ψ) improved our understanding of chain length effects on the capacitive performance of supercapacitors. Consistent with previous studies (Lian et al., 2016a; He et al., 2015; Rochester et al., 2016; Wu et al., 2012), the differential capacitance is the largest when the pore is near neutral since the exchange of ions provides the maximum net charge. Since counterions adsorption is the mechanism at play when the pore is highly charged, it is understandable that the capacitance in Fig. 9 decreases as the with voltage increases.

When the pore is negatively charged, counterions adsorption becomes the main charging mechanism with the ion exchange limitation, as mentioned previously, because the chains provide more hindrance to the adsorption for increased chain length. Even when ion exchange does occur, the frequency of multiple anions being removed will be reduced when most of the anions have already been depleted. Thus, this process will be more frequent for EMIM, and less frequent for HMIM, which is demonstrated by the comparison of the capacitance values.

However, when the pore is near neutral, ion exchange is the main driving mechanism in the charging of the pore. Since the exchange of three anions with HMIM will lead to a greater net charge change, the increase in capacitance for longer chain lengths can be understood.

Finally, when the pore is positively charged, the differential capacitance curves become nearly indistinguishable for all cases since the main driving force is anion adsorption. Counterions adsorption results in less capacitance because the net charge change is smaller than that of ion exchange. The similarity in differential capacitance can be attributed to similar processes occurring for all three systems since the anion is the same for each RTIL. However, if we were to zoom in on the three curves, the differen-

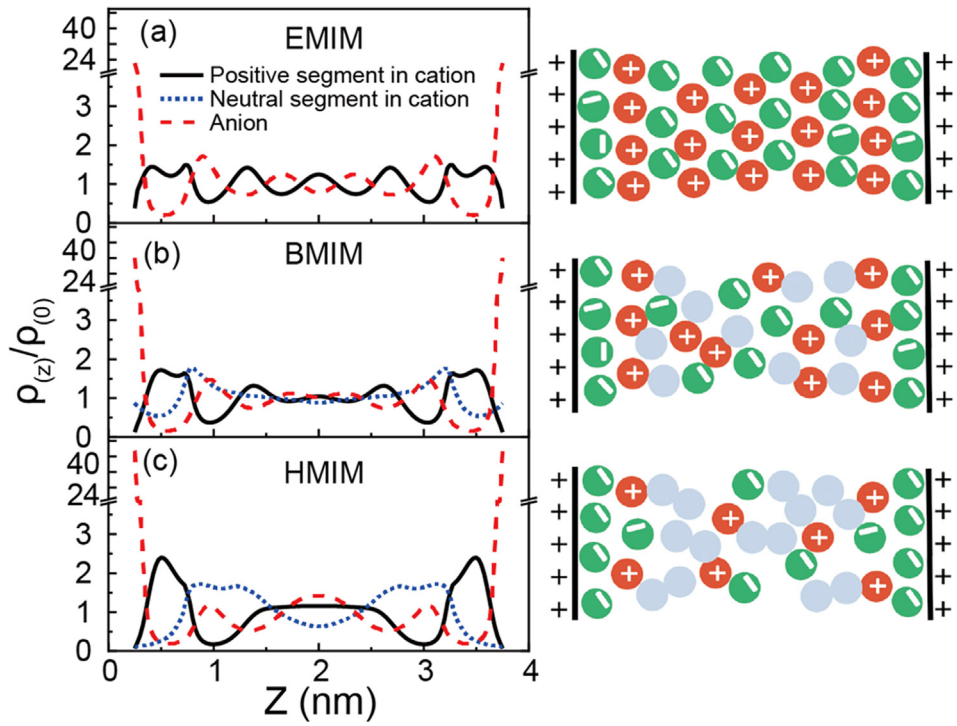

Fig. 6. Density profiles of anions (red dashed line) and the positive (black solid line) and neutral (blue dotted line) segments of cations inside a positively charged nanopore at the electrical surface potential of ψ for RTILs containing EMIM (a), BMIM (b), and HMIM (c). (For interpretation of the references to colour in this figure legend, the reader is referred to the web version of this article.)

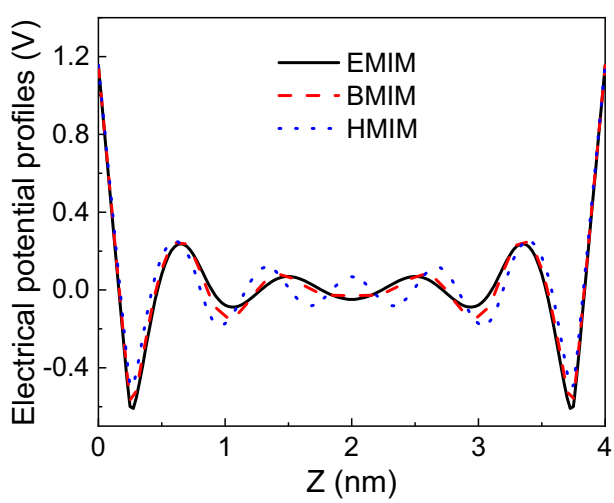

Fig. 7. Electrical potential profiles inside a positive nanopore at the electrical surface potential of ψ for RTILs containing EMIM (blue dotted line), BMIM (red dashed line), and HMIM (black solid line). (For interpretation of the references to colour in this figure legend, the reader is referred to the web version of this article.)

tial capacitance does decrease with increasing chain length. The reason is similar to that for the negatively charged system. If the mechanism at play involves few coion desorption, the desorption of HMIM is more difficult than that of a monomer.

4. Conclusions

In summary, additional neutral segments significantly change the interfacial structure and the capacitive behavior of EDLCs.

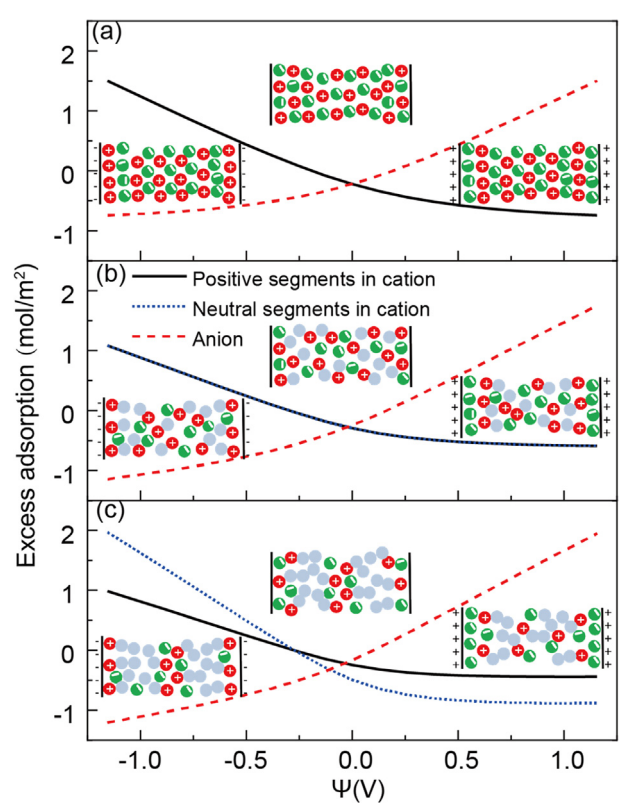

Fig. 8. Excess adsorption of anions (red dashed line) and the positive (black solid line) and neutral (blue dotted line) segments of cations inside the nanopore versus the electrical surface potential for RTILs containing EMIM (a), BMIM (b), and HMIM (c). (For interpretation of the references to colour in this figure legend, the reader is referred to the web version of this article.)

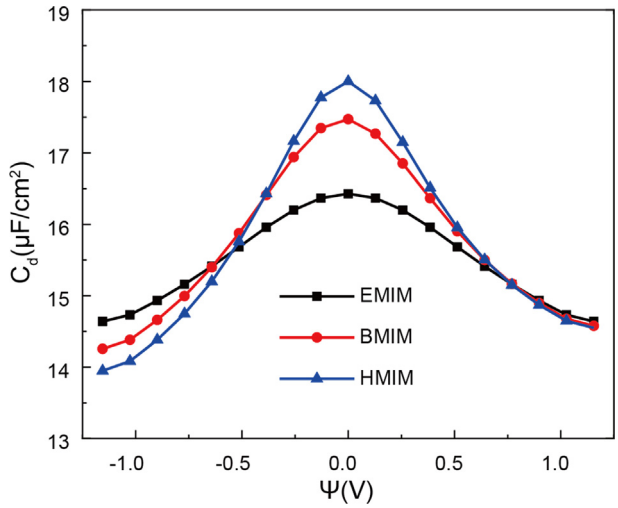

Fig. 9. Differential capacitance as a function of electrical surface potential for RTILs containing EMIM (black), BMIM (red), and HMIM (blue). (For interpretation of the references to colour in this figure legend, the reader is referred to the web version of this article.)

Specially, RTILs with shorter cations (a shorter neutral chain) form alternating layers of cations and anions, while longer cations (a longer neutral chain) lead to the formation of a new layer of neutral segments, which is consistent with previous experimental observations. The additional neutral chain disrupts the layering of ions that is normally seen for symmetrical ionic liquids as the neutral segments will occupy the space surrounding the cations and smooth the oscillation of charge and the bulk-like condition will be reached much sooner than that for the symmetrical system.

The use of cations with longer chains provides a greater net charge change in the exchange of ions such that the capacitance is significantly enhanced in nearly neutral pores. On the other hand, cations with longer chains dampen capacitance under negative electrical potential and show few disadvantages when positive potential is applied since they impede the adsorption/desorption of cations. Our theoretical results expand the understanding of the self-assembly of cations in nanoporous electrodes and the effects of neutral chains on the EDL structure and capacitance. We hope that this work will inspire future experimental and computational efforts in these directions.

CRediT authorship contribution statement

Jie Yang: Investigation, Visualization, Data curation, Formal analysis, Writing - original draft, Writing - review & editing. **Cheng Lian:** Conceptualization, Methodology, Software, Formal analysis, Writing - review & editing. **Honglai Liu:** Writing - review & editing, Supervision.

Declaration of Competing Interest

The authors declare that they have no known competing financial interests or personal relationships that could have appeared to influence the work reported in this paper.

Acknowledgments

This work was sponsored by the National Natural Science Foundation of China (No. 91834301 and 21808055), the Shanghai Sailing Program (18YF1405400). We kindly thank Alejandro Gallegos for helpful discussions.

References

Adusei, P.K., Gbordzoe, S., Kanakaraj, S.N., Hsieh, Y.-Y., Alvarez, N.T., Fang, Y., Johnson, K., McConnell, C., Shanov, V., 2020. Fabrication and study of supercapacitor electrodes based on oxygen plasma functionalized carbon nanotube fibers. J. Energy Chem. 40, 120–131. https://doi.org/10.1016/j.jechem.2019.03.005.

Bazant, M.Z., Storey, B.D., Kornyshev, A.A., 2011. Double layer in ionic liquids: overscreening versus crowding. Phys. Rev. Lett. 106, 046102. https://doi.org/10.1103/PhysRevLett.106.046102.

Burt, R., Birkett, G., Zhao, X.S., 2014. A review of molecular modelling of electric double layer capacitors. PCCP 16, 6519–6538. https://doi.org/10.1039/c3cp55186e.

Chmiola, J., Yushin, G., Gogotsi, Y., Portet, C., Simon, P., Taberna, P.L., 2006. Anomalous increase in carbon capacitance at pore sizes less than 1 nanometer. Science 313, 1760. https://doi.org/10.1126/science.1132195.

Chu, M., Miller, M., Dutta, P., 2016. Crowding and anomalous capacitance at an electrode-ionic liquid interface observed using operando X-ray scattering. ACS Cent. Sci. 2, 175–180. https://doi.org/10.1021/acscentsci.6b00014.

Dou, Q., Liu, L., Yang, B., Lang, J., Yan, X., 2017. Silica-grafted ionic liquids for revealing the respective charging behaviors of cations and anions in supercapacitors. Nature Commun. 8, 2188. https://doi.org/10.1038/s41467-017-02152-5.

Fedorov, M.V., Kornyshev, A.A., 2014. Ionic liquids at electrified interfaces. Chem. Rev. 114, 2978–3036. https://doi.org/10.1021/cr400374x.

Fedorov, M.V., Kornyshev, A.A., 2008a. Ionic liquid near a charged wall: structure and capacitance of electrical double layer. J. Phys. Chem. B 112, 11868–11872. https://doi.org/10.1021/jp803440q.

Fedorov, M.V., Kornyshev, A.A., 2008b. Towards understanding the structure and capacitance of electrical double layer in ionic liquids. Electrochim. Acta 53, 6835–6840. https://doi.org/10.1016/j.electacta.2008.02.065.

Feng, G., Zhang, J.S., Qiao, R., 2009. Microstructure and capacitance of the electrical double layers at the interface of ionic liquids and planar electrodes. J. Phys. Chem. C 113, 4549–4559. https://doi.org/10.1021/jp809900w.

Forsman, J., Woodward, C.E., Trulsson, M., 2011. A classical density functional theory of ionic liquids. J. Phys. Chem. B 115, 4606–4612. https://doi.org/10.1021/jp111747w.

Frackowiak, E., Abbas, Q., Béguin, F., 2013. Carbon/carbon supercapacitors. J. Energy Chem. 22, 226–240. https://doi.org/10.1016/S2095-4956(13)60028-5.

Gallegos, A., Lian, C., Dyatkin, B., Wu, J., 2019. Side-chain effects on the capacitive behaviour of ionic liquids in microporous electrodes. Mol. Phys. 117, 3603–3613. https://doi.org/10.1080/00268976.2019.1650210.

He, Y., Huang, J., Sumpter, B.G., Kornyshev, A.A., Qiao, R., 2015. Dynamic charge storage in ionic liquids-filled nanopores: insight from a computational cyclic voltammetry study. J. Phys. Chem. Lett 9.

Izgorodina, E.I., Forsyth, M., MacFarlane, D.R., 2009. On the components of the dielectric constants of ionic liquids: ionic polarization?. PCCP 11, 2452. https://doi.org/10.1039/b815835e.

Jiang, D., Meng, D., Wu, J., 2011. Density functional theory for differential capacitance of planar electric double layers in ionic liquids. Chem. Phys. Lett. 504, 153–158. https://doi.org/10.1016/j.cplett.2011.01.072.

Jiang, D.E., Wu, J., 2013. Microscopic insights into the electrochemical behavior of nonaqueous electrolytes in electric double-layer capacitors. J. Phys. Chem. Lett. 4, 1260–1267. https://doi.org/10.1021/jz4002967.

Jin, Z., Tang, Y., Wu, J., 2011. A perturbative density functional theory for square-well fluids. The J. Chem. Phys. 134, 174702. https://doi.org/10.1063/1.3585677.

Kondrat, S., Georgi, N., Fedorov, M.V., Kornyshev, A.A., 2011. A superionic state in nano-porous double-layer capacitors: insights from Monte Carlo simulations. PCCP 13, 11359–11366. https://doi.org/10.1039/C1CP20798A.

Kondrat, S., Kornyshev, A., 2011. Superionic state in double-layer capacitors with nanoporous electrodes. J. Phys.: Condens. Matter 23, 022201. https://doi.org/10.1088/0953-8984/23/2/022201.

Kondrat, S., Kornyshev, A.A., 2016. Pressing a spring: what does it take to maximize the energy storage in nanoporous supercapacitors?. Nanoscale Horiz. 1, 45–52. https://doi.org/10.1039/C5NH00004A.

Kumaravadivel, R., Evans, R., 1975. Calculations of the surface energy of simple liquid metals. J. Phys. C: Solid State Phys. 8, 793–808. https://doi.org/10.1088/0022-3719/8/6/010.

Largeot, C., Portet, C., Chmiola, J., Taberna, P.-L., Gogotsi, Y., Simon, P., 2008. Relation between the ion size and pore size for an electric double-layer capacitor. J. Am. Chem. Soc. 130, 2730–2731. https://doi.org/10.1021/ja7106178.

Li, Z., Wu, J., 2006a. Density functional theory for planar electric double layers: closing the gap between simple and polyelectrolytes. J. Phys. Chem. B 110, 7473–7484. https://doi.org/10.1021/jp060127w.

Li, Z., Wu, J., 2006b. Density functional theory for polyelectrolytes near oppositely charged surfaces. Phys. Rev. Lett. 96, 048302. https://doi.org/10.1103/PhysRevLett.96.048302.

Lian, C., Janssen, M., Liu, H., van Roij, R., 2020. Blessing and curse: how a supercapacitor's large capacitance causes its slow charging. Phys. Rev. Lett. 124, 076001. https://doi.org/10.1103/PhysRevLett.124.076001.

Lian, C., Liu, H., Henderson, D., Wu, J., 2016a. Can ionophobic nanopores enhance the energy storage capacity of electric-double-layer capacitors containing nonaqueous electrolytes?. J. Phys.: Condens. Matter 28, 414005. https://doi.org/10.1088/0953-8984/28/41/414005.

Lian, C., Liu, K., Liu, H., Wu, J., 2017. Impurity effects on charging mechanism and energy storage of nanoporous supercapacitors. J. Phys. Chem. C 121, 14066–14072. https://doi.org/10.1021/acs.jpcc.7b04869.

Lian, C., Liu, K., Van Aken, K.L., Gogotsi, Y., Wesolowski, D.J., Liu, H.L., Jiang, D.E., Wu, J.Z., 2016b. Enhancing the capacitive performance of electric double-layer capacitors with ionic liquid mixtures. ACS Energy Lett. 1, 21–26. https://doi.org/10.1021/acsenergylett.6b00010.

Lian, C., Su, H., Liu, H., Wu, J., 2018. Electrochemical behavior of nanoporous supercapacitors with oligomeric ionic liquids. J. Phys. Chem. C 122, 14402–14407. https://doi.org/10.1021/acs.jpcc.8b04464.

Liu, K., Zhang, P., Wu, J., 2018. Does capillary evaporation limit the accessibility of nonaqueous electrolytes to the ultrasmall pores of carbon electrodes?. J. Chem. Phys. 149, 234708. https://doi.org/10.1063/1.5064360.

Mezger, M., Schroder, H., Reichert, H., Schramm, S., Okasinski, J.S., Schoder, S., Honkimaki, V., Deutsch, M., Ocko, B.M., Ralston, J., Rohwerder, M., Stratmann, M., Dosch, H., 2008. Molecular layering of fluorinated ionic liquids at a charged sapphire (0001) surface. Science 322, 424–428. https://doi.org/10.1126/science.1164502.

Rochester, C.C., Kondrat, S., Pruessner, G., Kornyshev, A.A., 2016. Charging ultrananoporous electrodes with size-asymmetric ions assisted by apolar solvent. J. Phys. Chem. C 120, 16042–16050. https://doi.org/10.1021/acs.jpcc.5b12730.

Rosenfeld, Y., 1989. Free-energy model for the inhomogeneous hard-sphere fluid mixture and density-functional theory of freezing. Phys. Rev. Lett. 63, 980–983. https://doi.org/10.1103/PhysRevLett.63.980.

Seddon, K.R., 1997. Ionic liquids for clean technology. J. Chem. Tech. Biotech. 68, 351–356. https://doi.org/10.1002/(SICI)1097-4660(199704)68:4<351::AID-JCTB613>3.0.CO;2-4.

Shao, Y., El-Kady, M.F., Wang, L.J., Zhang, Q., Li, Y., Wang, H., Mousavi, M.F., Kaner, R. B., 2015. Graphene-based materials for flexible supercapacitors. Chem. Soc. Rev. 44, 3639–3665. https://doi.org/10.1039/c4cs00316k.

Shrivastav, G., Remsing, R.C., Kashyap, H.K., 2018. Capillary evaporation of the ionic liquid [EMIM][BF4] in nanoscale solvophobic confinement. J. Chem. Phys. 148, 193810. https://doi.org/10.1063/1.5010259.

Simon, P., Gogotsi, Y., 2013. Capacitive energy storage in nanostructured carbon-electrolyte systems. Acc. Chem. Res. 46, 1094–1103. https://doi.org/10.1021/ar200306b.

Simon, P., Gogotsi, Y., 2008. Materials for electrochemical capacitors. Nature Mat. 7, 845–854. https://doi.org/10.1038/nmat2297.

Smith, A.M., Lovelock, K.R.J., Gosvami, N.N., Licence, P., Dolan, A., Welton, T., Perkin, S., 2013. Monolayer to bilayer structural transition in confined pyrrolidinium-based ionic liquids. J. Phys. Chem. Lett. 4, 378–382. https://doi.org/10.1021/jz301965d.

Smith, A.M., Parkes, M.A., Perkin, S., 2014. Molecular friction mechanisms across nanofilms of a bilayer-forming ionic liquid. J. Phys. Chem. Lett. 5, 4032–4037. https://doi.org/10.1021/jz502188g.

Szparaga, R., Woodward, C.E., Forsman, J., 2012. Theoretical prediction of the capacitance of ionic liquid films. J. Phys. Chem. C 116, 15946–15951. https://doi.org/10.1021/jp3053357.

Valderrama, J.O., Rojas, R.E., 2009. Critical properties of ionic liquids. Revisited. Ind. Eng. Chem. Res. 48, 6890–6900. https://doi.org/10.1021/ie900250g.

van Roij, R., Dijkstra, M., Hansen, J.-P., 1999. Phase diagram of charge-stabilized colloidal suspensions: van der Waals instability without attractive forces. Phys. Rev. E 59, 2010–2025. https://doi.org/10.1103/PhysRevE.59.2010.

Wang, Z.-Y., 2016. Image-induced overcharging in the weakly charged surfaces. J. Stat. Mech. 2016, 043205. https://doi.org/10.1088/1742-5468/2016/04/043205.

Wertheim, M.S., 1984. Fluids with highly directional attractive forces. I. Statistical thermodynamics. J. Stat. Phys. 35, 19–34. https://doi.org/10.1007/BF01017362.

Wu, J., 2006. Density functional theory for chemical engineering: from capillarity to soft materials. AIChE J. 52, 1169–1193. https://doi.org/10.1002/aic.10713.

Wu, J., Jiang, T., Jiang, D., Jin, Z., Henderson, D., 2011. A classical density functional theory for interfacial layering of ionic liquids. Soft Matter 7. https://doi.org/10.1039/c1sm06089a.

Wu, P., Huang, J., Meunier, V., Sumpter, B.G., Qiao, R., 2012. Voltage dependent charge storage modes and capacity in subnanometer pores. J. Phys. Chem. Lett. 3, 1732–1737. https://doi.org/10.1021/jz300506j.

Yu, Y.-X., Wu, J., 2002a. Structures of hard-sphere fluids from a modified fundamental-measure theory. J. Chem. Phys. 117, 10156–10164. https://doi.org/10.1063/1.1520530.

Yu, Y.-X., Wu, J., 2002b. A fundamental-measure theory for inhomogeneous associating fluids. J. Chem. Phys. 116, 7094–7103. https://doi.org/10.1063/1.1463435.

Yu, Y.X., Wu, J., Gao, G.H., 2004. Density-functional theory of spherical electric double layers and zeta potentials of colloidal particles in restricted-primitive-model electrolyte solutions. J. Chem. Phys. 120, 7223–7233. https://doi.org/10.1063/1.1676121.

Zhong, C., Deng, Y., Hu, W., Qiao, J., Zhang, L., Zhang, J., 2015. A review of electrolyte materials and compositions for electrochemical supercapacitors. Chem. Soc. Rev. 44, 7484–7539. https://doi.org/10.1039/c5cs00303b.